Enzymatically produced cellulose nanocrystals as reinforcement for waterborne polyurethane and its applications

Borja Alonso-Lerma[1,2], Izaskun Larraza[1], Leire Barandiaran[2], Lorena Ugarte[1], Ainara Saralegi[1], Maria Angeles Corcuera[1], Raul Perez-Jimenez[2,3,4]* & Arantxa Eceiza[1]*

[1.]*Group 'Materials + Technologies', Department of Chemical and Environmental Engineering, Faculty of Engineering of Gipuzkoa, University of the Basque Country, San Sebastian, Spain.*

[2.]*CIC nanoGUNE BRTA, San Sebastian, Spain.*

[3.]*Ikerbasque Foundation for Science, Bilbao, Spain.*

[4.]*Evolgene Genomics S.L., San Sebastian, Spain*

*Corresponding authors E-mail: arantxa.eceiza@ehu.eus & r.perezjimenez@nanogune.eu

ABSTRACT

Waterborne polyurethanes (WBPUs) have been proposed as ecofriendly elastomers with several applications in coatings and adhesives. WBPU´s physicochemical properties can be enhanced by the addition of cellulose nanocrystals (CNCs). The way CNCs are isolated has a strong effect on their properties and can determine their role as reinforcement. In this work, CNCs produced using ancestral endoglucanase (EnCNCs) were used as reinforcement for WBPU and compared with CNC produced by sulfuric acid hydrolysis (AcCNC). The enzymatic method produced highly thermostable and crystalline CNCs. The addition of small contents of EnCNCs improved the thermomechanical stability and mechanical properties of WBPUs, even better than commercial AcCNCs. Besides, WBPU reinforced by adding EnCNCs was studied as a coating for paper materials, increasing its abrasion resistance and as electrospun nanocomposite mats where EnCNCs helped maintaining the morphology of the fibers.

Keywords: Cellulose nanocrystals; Enzymatic hydrolysis; Waterborne polyurethane, Nanocomposite reinforcement.

1. Introduction

The current concern about climate change and the need to reduce the pollution and waste amount towards a sustainable development in the fields of polymeric materials manufacturing and manipulation, are boosting the attention of researchers on the search of eco-friendly alternatives. This is the case of aqueous dispersions based on hydrophobic polymers like polyurethanes, also known as waterborne polyurethanes (WBPUs). WBPUs can gather stable particles in aqueous dispersions by adding covalently bonded internal emulsifiers, thus avoiding the use of toxic organic solvents in their manipulation (Nelson & Long, 2014; Voronova, Surov, Guseinov, Barannikov, & Zakharov, 2015). Furthermore, WBPUs synthesis can be based on bio-based raw materials (Remya, Patil, Abitha, Rane, & Mishra, 2016) (Lu & Larock, 2008; Madbouly, Xia, & Kessler, 2013).

WBPUs are block copolymers formed by two blocks or segments, the hard segment (HS), formed by a diisocyanate, a chain extender, and an emulsifier, and the soft segment (SS), composed of a polyol (Jaudouin, Robin, Lopez-Cuesta, Perrin, & Imbert, 2012). These segments are usually thermodynamically incompatible and result in microphase separated phases or domains. Usually, SS makes the material flexible, and HS provides stiffness, but both segments can be ordered into amorphous or crystalline domains modulated by hydrogen bonding interactions. Therefore, WBPUs have high strength and flexibility related to the hard and soft segments, as well as the microphase separated structure (Saralegi et al., 2013; Yang & Wu, 2020). WBPUs have different applications as elastomers (Urbina et al., 2019), coatings (Rahman, Suleiman, & Do Kim, 2017; Rahman, Zahir, Haq, Shehri, & Kumar, 2018), adhesives (Perez-Liminana, Aran-Ais, Torró-Palau, Orgilés-Barceló, & Martín-Martínez, 2005), and even in biomedical applications due to its biocompatibility (Hung, Tseng, Dai, & Hsu, 2016; Yoo & Kim, 2008). Moreover, WBPUs' mechanical and thermal properties such as stiffness, toughness, and thermomechanical stability can be improved by adding a reinforcement such as cellulose nanocrystals (CNCs) (Chowdhury et al., 2019; Gao et al., 2012; M. E. V. Hormaiztegui, Daga, Aranguren, & Mucci, 2020; M. V. Hormaiztegui, Mucci, & Aranguren, 2019; Lei, Zhou, Fang, Song, & Li, 2019; Mondragon et al., 2018; Santamaria-Echart, Ugarte, Arbelaiz, et al., 2016; Santamaria-Echart, Ugarte, García-Astrain, et al., 2016; Saralegi, Gonzalez, Valea, Eceiza, & Corcuera, 2014).

CNCs have aroused the attention of the scientific community since its implementation produces more cost-effective, durable, and greener materials. CNCs are widely used due to

their extraordinary properties, such as biocompatibility, renewability, sustainability, and thermal and mechanical behavior (Dufresne, 2013; Habibi, Lucia, & Rojas, 2010). CNCs are small crystalline particles with diameters of 3-40 nm and lengths around 100-500 nm, depending on the cellulosic source and isolation method (Trache, Hussin, Haafiz, & Thakur, 2017). The higher crystallinity that CNCs present comparing to cellulose nanofibers (NFCs) results in higher specific mechanical properties, which can be compared with other nanomaterials such as carbon nanotubes (Moon, Martini, Nairn, Simonsen, & Youngblood, 2011).

CNCs can be isolated by different methods as mechanical (Amin, Annamalai, Morrow, & Martin, 2015), chemical (Kallel et al., 2016), enzymatic (Filson, Dawson-Andoh, & Schwegler-Berry, 2009), or combinations of them (Henriksson, Henriksson, Berglund, & Lindström, 2007; Yarbrough et al., 2017). The isolation process has different effects on the crystals' physicochemical properties, modifying its structure, crystallinity, thermal stability, or even attaching new functional groups to the crystal surface through covalent functionalization. Surface functionalization also has a dramatic effect on their properties (Lin & Dufresne, 2014). In a previous work, the isolation of CNCs by an eco-friendly method based on enzymatic hydrolysis (EnCNCs) using an ancestral endoglucanase was optimized, producing CNCs with higher crystallinity and thermal stability compared to commercial CNCs produced by sulfuric acid hydrolysis (AcCNC) (Borja Alonso-Lerma et al., 2020). AcCNCs have been widely used as reinforcement with different polymers such as polycarbonate (PC) (Park et al., 2019), polyvinyl alcohol (PVA) (Voronova et al., 2015), polylactic acid (PLA) (Fortunati et al., 2012), polymethylmethacrylate (Liu, Liu, Yao, & Wu, 2010), natural rubber (Jardin, Zhang, Hu, Tam, & Mekonnen, 2020). On the contrary, CNC produced only by enzymatic methods (EnCNC) has not been implemented yet, neither to reinforce WBPU where AcCNC has been used in previous works (Santamaria-Echart, Ugarte, Arbelaiz, et al., 2016).

In this work, to analyze the effect of the isolation method and CNCs physicochemical properties over the nanocomposite's performance, strong and transparent nanocomposites composed of WBPU matrix and different contents of EnCNCs and AcCNCs were prepared. Nanocomposites were characterized from their physicochemical, thermal, mechanical, and morphological properties by Fourier Transform Infrared spectroscopy (FTIR), Differential Scanning Calorimetry (DSC), Dynamic Mechanical Analysis (DMA), Water Contact Angle (WCA), mechanical testing, Thermogravimetric analysis (TGA), Scanning Electron

93   Microscopy (SEM) and Atomic Force Microscopy (AFM). Moreover, two different

94   applications were investigated; coatings for a paper substrate and hybrid dispersions for the

95   fabrication of electrospun based microfiber mats, to compare the performance of these

96   WBPU/EnCNC and WBPU/AcCNC formulations and prove the versatility and enhancement

97   of properties with the use of EnCNCs.

98   2. Materials and methods

99   2.1. Materials

100   For enzymatically isolated cellulose nanocrystals with endoglucanase, denoted as EnCNC,

101   Whatman® filter paper was used as a substrate. Cellulose nanocrystals produced by sulfuric

102   acid treatment and purchased from Maine University in freeze dried form (0.94 wt% sulfur on

103   sodium form) (Lot# 2014-FPL-CNC-065) were used for comparison and named as AcCNC.

104   For the synthesis of the biobased waterborne poly (urethane-urea) dispersion, a difunctional

105   macrodiol derived from renewable sources, Priplast 3192® (Mw= 2000 g mol^{-1}), purchased

106   from Croda, was used as the soft segment. Isophorone diisocyanate (IPDI), kindly supplied by

107   Covestro, 2,2-bis (hydroxymethyl) propionic acid (DMPA) as internal emulsifier and provided

108   by Aldrich, and ethylenediamine (EDA) as chain extender and provided by Fluka, were used

109   as hard segment. Triethylamine (TEA), supplied by Fluka, was employed to neutralize the

110   carboxylic groups of the internal emulsifier, leading to ionic groups in the surface of the

111   dispersed particles. Dibutyltin dilaurate (DBTDL), purchased from Aldrich, was used as a

112   catalyst. Both the polyol and the DMPA were dried under vacuum at 60 °C for 4 hours before

113   their use.

114   2.2. Protein expression and purification.

115   ANC EG+CBM protein-encoding gene was synthesized and codon-optimized for *E.coli*

116   cell expression following a previously published protocol (B Alonso-Lerma et al., 2020).

117   Briefly, ANC EG+CBM was cloned in pQE80L expression vector (Qiagen) and transformed

118   in E. coli BL21 (DE3) (Life Technologies) for protein expression. Cells were incubated in LB

119   medium at 37 °C until OD$_{600}$ reached 0.6. Isopropyl β-D-1-thiogalactopyranoside (IPTG) was

120   added to the medium at 1 mM concentration for protein induction overnight. Cells were

121   pelleted by centrifugation at 4000 rpm. Pellets were resuspended in an extraction buffer (50

122   mM sodium phosphate, pH 7.0, 300 mM NaCl) and mechanically lysed using French Press.

123   Cell debris was separated by ultracentrifugation at 33000 G for 1 hour. For purification, the

124 supernatants were mixed with His GraviTrap affinity column (GE Healthcare) and eluted in an

125 elution buffer (50 mM sodium phosphate, pH 7.0, 300 mM NaCl, 150 mM imidazole). Proteins

126 were further purified by size exclusion chromatography using a Superdex 200 HR column (GE

127 Healthcare) and eluted in 50 mM citrate buffer (26 mM Sodium Citrate dihydrate, 24 mM Citric

128 Acid, pH 4.8). For the verification of the protein purification, sodium dodecyl sulfate-

129 polyacrylamide gel electrophoresis (SDS-PAGE) was used with 12% gels. The protein

130 concentration was calculated by measuring the absorbance at 280 nm in Nanodrop 2000C

131 spectrophotometer.

132 2.3. Enzymatically produced cellulose nanocrystals.

133 Whatman® filter paper dispersed in water (1% w/v) was used for nanocrystal production,

134 chopped in small squares of 1 cm^2. The reaction was carried out in water, and 5 mg of ANC

135 EG+CBM were used per gram of substrate. Hydrolysis was incubated at 50 ℃ in agitation for

136 24 hours. The reaction was stopped by incubating the hydrolysis on ice, and the mixture was

137 sonicated with a microtip sonicator UPH100H Ultrasonic Processor (Hielscher) for 25 min at

138 75%. Nanocrystals were isolated by gradual centrifugation steps and concentrated by

139 ultracentrifugation at 33000 G for 1 hour. Pellets were resuspended in water and maintained at

140 4 ℃ until their use.

141 2.4. Synthesis of waterborne polyurethanes.

142 A WBPU was synthesized using a two-step polymerization procedure in a 250 mL four-

143 necked flask equipped with a mechanical stirrer, thermometer, and nitrogen inlet, as well as a

144 thermostatic bath. In the first step, the prepolymer, composed of the macrodiol, internal

145 emulsifier, and the diisocyanate, was synthesized, and in the second step, the chain extension

146 was carried out. The reaction progress was monitored using the dibutylamine back titration

147 method, according to ASTM D 2572-97. In the first step of the reaction, the macrodiol, IPDI,

148 and 0.037 wt% of DBTL respect to the prepolymer content were reacted at 100 ℃ for 5 hours

149 under mechanical stirring. Then, the DMPA neutralized with TEA and dissolved in a little

150 amount of acetone was added at 50 ℃ and left to react for 1 more hour. The system was then

151 cooled down to room temperature, where the phase inversion step was carried out by adding

152 dropwise the deionized water under vigorous stirring. In the second step of the synthesis, the

153 chain extender (EDA) was added at room temperature. The mixture was allowed to react for 2

154 hours at 35 ℃ under stirring, forming the waterborne polyurethane dispersion with a solid

content of 33 wt%. The resulting WBPU was synthesized using a molar ratio of macrodiol/DMPA/IPDI/EDA of 1/1.1/3.5/0.6.

2.5. WBPU/CNC nanocomposite films.

Nanocomposite films based on the synthesized WBPU and different contents of EnCNCs and AcCNCs were prepared by solvent casting method. CNCs aqueous suspensions were sonicated at room temperature for 1 hour, and after the addition of WBPU, the mixtures were sonicated for 1 more hour. Mixtures of 45 mL were prepared, adjusting the volume with the extra addition of water in those cases where the CNCs content was low. The mixtures were cast in Teflon molds, dried first at room temperature for 7 days, and then under vacuum at 25 ℃ for 3 days. Films were stored in a desiccator one week before their characterization. Films with a thickness of around 0.4 mm containing 1, 3, 5, and 7 wt% of EnCNC and AcCNC were prepared. Nanocomposites were named as "WBPU x% EnCNC" and "WBPU x% AcCNC" where "x" was the content of EnCNC and AcCNC (wt%) with respect to the total mass of the composite. **Fig. 1** shows a scheme of the nanocomposite's preparation protocol. Transparent nanocomposite films were obtained, and no differences were found in the appearance of the films prepared with either EnCNCs or AcCNCs.
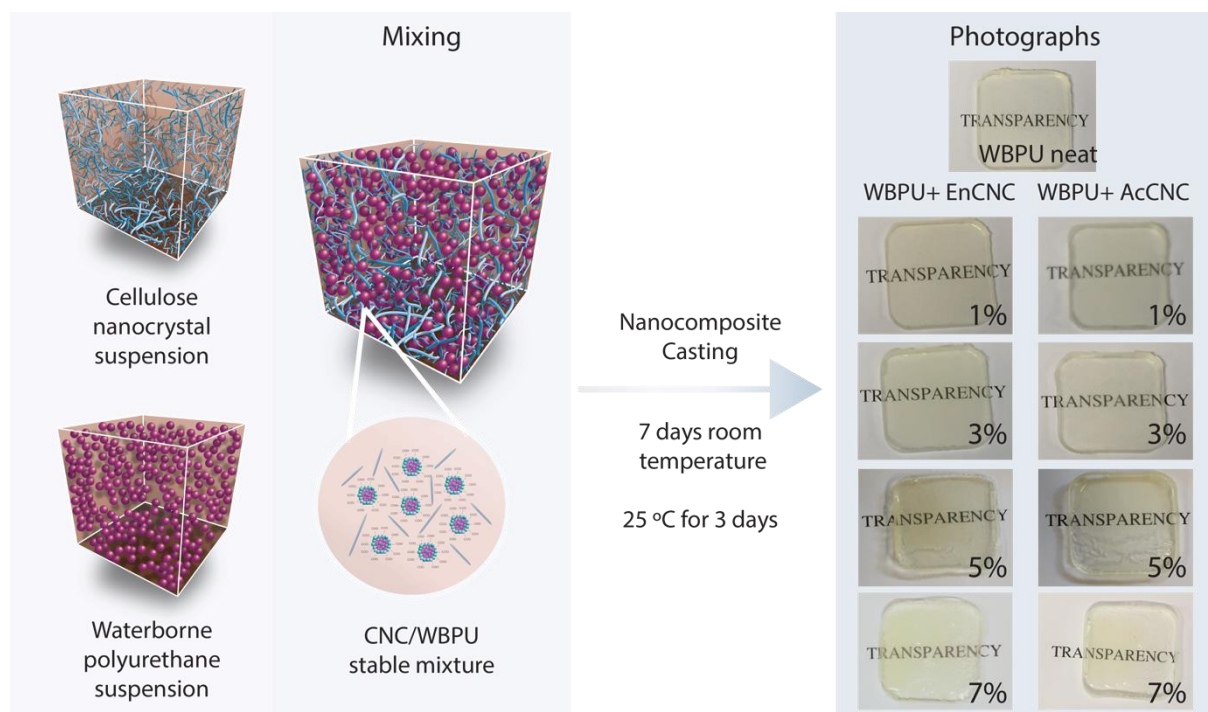
Fig. 1. Fabrication of WBPU/CNC nanocomposites with different EnCNC and AcCNC contents.

174   2.6. WBPU/CNC coatings.

The same WBPU/CNC formulations prepared, as described previously, were used to apply
different coating layers over the satin paper manually. To apply the coating, the Green K-bar
(K bars®, RK Print Coat Instruments Ltd., United Kingdom) made of steel was used to produce
a wet film of 24 µm. The coating was applied over the paper and let it dry at 50 ºC for 1 hour.
The process was repeated to fabricate coatings of 1, 2, and 3 layers of each formulation.

180   2.7. WBPU/CNC electrospinning.

To fabricate nanocomposite electrospun mats, WBPU was mixed with 3 wt% of each type
of CNC and 4 wt% of polyoxyethylene (POE, 900.000 Da) to help material spinning. As a
control, a mixture of WBPU and POE was prepared. WBPU/CNC dispersions were sonicated
for 1 hour, and then POE was added and stirred to dissolve it for 24 hours. Mixtures were
loaded into a syringe, and spinning was performed with a FLUIDNATEK® LE-10 (Bioinicia)
spinning equipment. The collector was placed at 20 cm from the syringe needle. The hybrid
dispersion was released with a flow of 0.5 mL per hour, and 15 kV of voltage was applied.
Microfiber mats were collected in an aluminum foil for 1 hour. Finally, POE was removed
from the mats by submerging them in water for 24 hours, and finally, the mats were left
horizontally to dry out overnight at room temperature.

191   2.8. Dynamic light scattering.

The particle size of the WBPU dispersion and its distribution were measured by Dynamic
Light Scattering (DLS), using a BI-200SM goniometer from Brookhaven. The intensity of
dispersed light was measured using a luminous source of He-Ne laser (Mini L-30, wavelength
637 nm, 400 mW) and a detector (BI–APD) placed on a rotary arm, which allows measuring
the intensity at 90°. Samples were prepared, mixing a small amount of aqueous dispersions
with ultrapure water, and measurements were carried out at 25 ºC by triplicate.

198   2.9. Atomic force microscopy.

The morphology of nanocomposites was studied by AFM. Images were captured in tapping
mode at room temperature, using a Nanoscope V scanning probe microscope (Multimode 8
Bruker Digital Instruments) with an integrated force generated by cantilever/silicon probes.
The applied resonance frequency was 320 kHz. The cantilever had a tip radius of 5-10 nm and
was 125 µm long. Samples were prepared by sonicating them for 1 hour before spin-coating

204   (Spincoater P6700) deposition at 2000 rpm for 130 s through casting a droplet of

205   nanocomposite dispersions on glass supports. Different zones were scanned to ensure that the

206   obtained morphology was the representative one. AFM height and phase images were collected

207   simultaneously.

208   2.10. Water contact angle.

209   The hydrophilicity of the WBPU and nanocomposite films' surface and the coated papers

210   and the electrospun mats were measured by static WCA using a Dataphysics OCA20

211   equipment at room temperature. A 3 µl drop of deionized water was deposited in the samples'

212   surface to analyze the contact angle value that the water drop formed, which depends on the

213   chemical interactions between the water and the material surface. WCA was measured 10

214   seconds after the drop touched the film. When the material is hydrophilic, the contact angle is

215   low and increases with the sample's hydrophobicity. The contact angle (θc) values of ten water

216   drops deposited by a syringe tip were averaged for each sample.

217   2.11. Fourier transform infrared spectroscopy.

218   The characteristic functional groups and chemical interactions between WBPU and different

219   CNC types in the nanocomposites and the electrospun mats were analyzed by FTIR. FTIR

220   spectroscopy measurements were recorded by a Nicolet Nexus spectrometer provided with a

221   MKII Golden Gate accessory (Specac) with a diamond crystal at a nominal incidence angle of

222   45° and ZnSe lens. Spectra were recorded in attenuated total reflection (ATR) mode between

223   4000 and 750 cm^{-1}, with averaging 32 scans with a resolution of 4 cm^{-1}.

224   2.12. Differential scanning calorimetry.

225   The thermal properties of the WBPU and nanocomposites were determined by DSC. The

226   analysis was performed using a Mettler Toledo DSC 822 equipment provided with a robotic

227   arm and an electric intracooler as refrigerator unit. Between 5 and 10 mg of sample were

228   encapsulated in aluminum pans and heated from -70 to 180 ℃ at a scanning rate of 10 ℃ min^{-}

229   ^{1} in nitrogen atmosphere. The glass transition temperature (T_{gSS}), determined as the inflection

230   point of the observed heat capacity change, the melting temperature of the soft segment (T_{mSS})

231   and the short range order transition of the hard segment (T_{HS}), taken as the maximum of the

232   endothermic peaks, and the enthalpy of the hard segment short range ordering (ΔH_{HS}),

233   determined from the area under the peak, were calculated from first heating thermograms.

234   2.13. Dynamic mechanical analysis.

235   The viscoelastic behavior of the films was investigated by DMA using an Eplexor 100 N

236   analyzer Gabo equipment. Samples were subjected to a sinusoidal strain, and the stress

237   response was measured by varying the temperature of the sample. Measurements were carried

238   out in tensile mode from -100 to 130 ℃ at a scanning rate of 2 ° C min^{-1}. The initial strain was

239   established at 0.05%, and the operating frequency was fixed at 1 Hz. The storage modulus (E´)

240   and the tangent of phase angle (Tanδ) of WBPU and nanocomposites were determined. The

241   maximum of Tan δ peak can be associated with the T_{gSS} of the sample and can also be followed,

242   observing a drop at the E´ curve simultaneously. Samples of 4 cm in length, 0.5 cm of width,

243   and 0.4 mm in thickness for WBPU and each nanocomposite were tested.

244   2.14. Mechanical test.

245   The mechanical performance of the WBPU and nanocomposites was measured at 22 ℃ and

246   50% of relative humidity. The samples were submitted to a constant elongation rate until they

247   broke. In this way, the equipment records each sample's elongation and force values and plots

248   them as stress-strain curves, from which Young modulus, tensile strength, strain at break, yield

249   strength, and toughness were determined. Tests were performed in an Instron 5967 testing

250   machine provided with a 500 N load cell and pneumatic grips to hold the samples, operating at

251   a crosshead speed of 50 mm min^{-1}. Samples of 4 cm in length, 0.5 cm of width, and 0.4 mm in

252   thickness for WBPU and each nanocomposite were employed. Five samples of WBPU and

253   each nanocomposite were tested, determining the average value and standard deviation for each

254   property.

255   2.15. Thermogravimetric analysis (TGA)

256   The analysis was performed using a TGA/SDTA 851 Mettler Toledo equipment. Up to 10

257   mg of the samples were used and were heated from 30 to 700 ℃ in a nitrogen atmosphere at a

258   scanning rate of 10 ℃/min.

259   2.16. Adhesion test.

260   The adhesion performance of the coatings over the paper was measured by cross-cut tape

261   adhesion tests. In that sense, coatings were cut with a multi-edge cutting tool (1 mm separation)

262   with a stable perpendicular force. The cut was repeated with a 90° angle to produce a pattern

263   of 100 small squares over the film. A brush was used to clean the surface, and then a 3 M tape

264 (ISO 2409) was stacked to the grid and pressed to produce proper adhesion. Finally, the tape

265 was peeled off. The squares were observed in an optical microscopy to quantify the peeling of

266 the coating according to ASTM D3359 standards charts[44]. The adhesion is graded according to

267 the 5B, 4B, 3B, 2B, 1B, and 0B scale, where 5B corresponds to the best adhesion and 0B to

268 the worst.

269 2.17. Abrasion test.

270 Abrasion resistance was evaluated employing a Taber abrader with two abrasive wheels CS-

271 10. The wheels were loaded with 250 g and rotated independently on the rotating platform at

272 60 rpm based on ASTM D4060 Taber standard. This quantitative method had been used in the

273 literature as a standard method for testing coatings (Standard, 2010; Zheng et al., 2019). The

274 papers were compared after 50 cycles of abrasion.

275 2.18. Scanning electron microscopy.

276 The cross-section of nanocomposites and the surface morphology of casted papers after

277 abrasion tests and electrospun mats was analyzed by SEM using a FEI ESEM Quanta 200

278 microscope operating at 5-20 kV at a low vacuum mode.

279 3. Results and discussion

280 3.1. Characterization of nanocrystals

281 In a previous work, a novel method for nanocrystal production based on enzymatic

282 hydrolysis was studied and optimized. Thus, the EnCNCs produced were characterized and

283 compared with commercial AcCNCs produced by sulfuric acid hydrolysis treatment. The

284 obtained results are summarized in **Fig. 1S**. AFM images revealed that EnCNCs were longer

285 in comparison with AcCNCs. EnCNCs measured around 408 ± 15.1 nm in length and $12.5 \pm$

286 0.8 nm in diameter, while AcCNCs measured 173 ± 6.3 nm in length and 10 ± 0.4 nm in

287 diameter. Therefore, EnCNCs had a higher aspect ratio, around 33, while the AcCNCs aspect

288 ratio was about 17. Moreover, EnCNCs and AcCNCs showed different morphologies. EnCNCs

289 showed needle-like morphology, while AcCNCs showed ribbon-like morphology. Both CNC

290 type chemical structures were analyzed by FTIR, XRD, and NMR. It was observed that

291 EnCNCs presented cellulose I pattern on FTIR, XRD and NMR analysis, while AcCNCs

292 pattern was assigned to a mixture of cellulose I and cellulose II. Besides, a crystallinity index

293 of 87.9% was measured for EnCNCs and 80.5% for AcCNCs sample. Regarding thermal

stability, it was analyzed by TGA. It was observed that AcCNCs presented lower thermal stability. The initial degradation temperature and maximum degradation temperature of EnCNCs were 262 and 356 ºC; meanwhile, for AcCNCs, they were 269 ºC and 298 ºC, respectively. These differences between CNCs were explained by the isolation method followed for their production. CNCs produced following a sulfuric acid-based hydrolysis treatment presented lower crystallinity and thermal stability due to the aggressiveness of the acidic hydrolysis treatment. Also, the treatment with sulfuric acid anchored OSO_3^- functional groups at the crystals' surface, owing to an esterification reaction during the hydrolysis process. This was confirmed by conductometric titration, measuring 0.95% of sulfur content for AcCNCs samples. This functional group is responsible for some specific properties of these CNCs.

3.2. Characterization of WBPU/CNC nanocomposites

The microstructure and macroscopic properties of nanocomposite films were analyzed to understand the influence of different CNC types and contents over the final properties and evaluate some tested applications of the prepared nanocomposites.

WBPU matrix morphology and the effect of CNC addition, both EnCNCs and AcCNCs, in the morphology of the nanocomposites were analyzed by AFM. Height and phase images of the WBPU matrix and nanocomposites with 5 wt% of EnCNCs and AcCNCs are displayed in **Fig. 2.a**. In the WBPU matrix height image, spherical nanoparticles with the expected size were observed, around 160 nm, which was also measured by dynamic light scattering. In samples with both types of CNCs, no nanocrystal agglomerations were observed, and the morphology presented for the WBPU matrix was maintained. Comparing the images of nanocomposites prepared with EnCNCs and AcCNCs, some differences in nanocrystals' arrangement were observed. EnCNCs were hard to distinguish in the matrix due to its longer size permits them to create an entangled structure within the matrix. In the case of AcCNCs, it seemed that they were less embedded in the matrix as they could be seen more clearly at the surface. Furthermore, EnCNC could have more free –OH groups to favored hydrogen bonding interactions with carboxylic, urea and urethane groups at the surface of WBPU nanoparticle than AcCNCs, due to the substitution of part of –OH groups with sulfate groups owing to the isolation treatment used, which could favor effective entanglements (Santamaria-Echart, Ugarte, García-Astrain, et al., 2016). The different interactions and locations that the two nanocrystals adopted during the casting procedure could explain the physicochemical and

326 mechanical behavior of the films. Nanocomposites cross-section was also observed by SEM

327 (**Fig. 2S**) where no CNC agglomerations were observed.
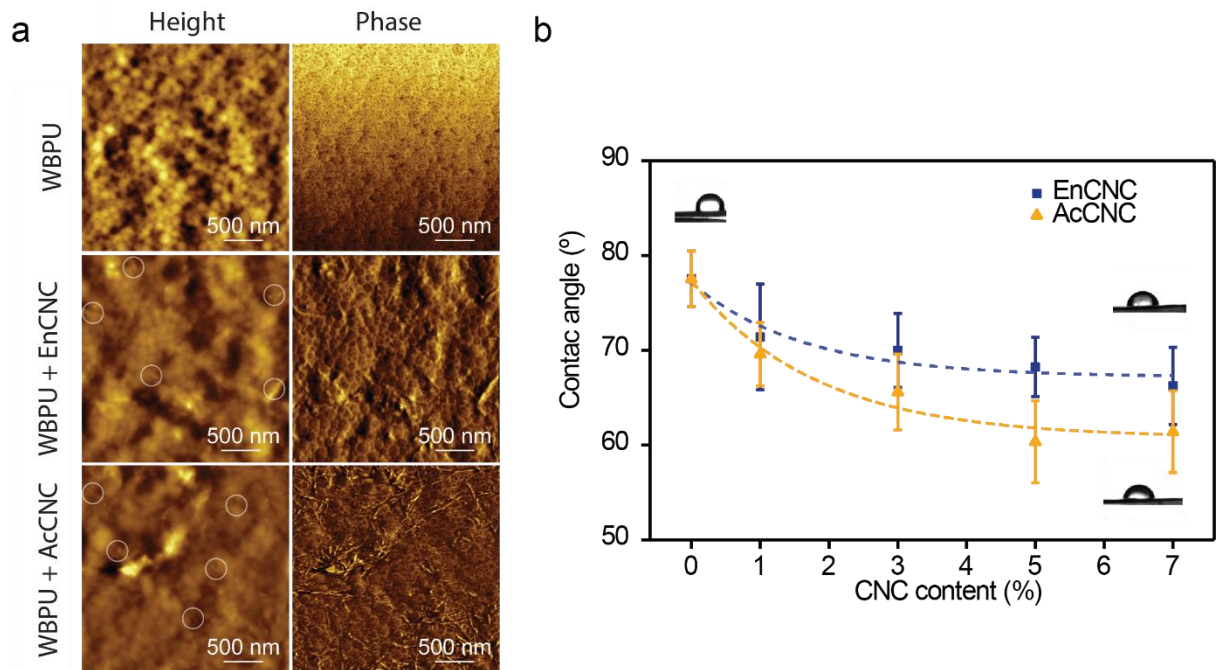
329 **Fig. 2. AFM analysis and water contact angle values of WBPU and WBPU/CNC**
330 **nanocomposites.** (a) AFM height and phase images (2 µm x 2 µm) of WBPU matrix and
331 WBPU nanocomposites with 5 wt% of EnCNCs and AcCNCs. Circles mark some CNCs
332 observed in the images. (b) Contact angle values of a water drop over the WBPU matrix
333 and nanocomposites with different EnCNC and AcCNC contents. The average contact
334 angle values and the standard deviations were calculated from ten independent
335 experiments.

336 The nanocomposites hydrophobicity was measured by WCA in order to analyze the CNC
337 effect in WBPU (**Fig. 2.b**). A reduction of the contact angle with the increase of CNC content
338 in both EnCNC and AcCNC based nanocomposites was observed; the lower the contact angle
339 of the water droplets on the surface of the sample to be analyzed, means that the material is
340 more hydrophilic. In EnCNC based nanocomposites, the water contact angle decreased sharply
341 until 1 wt% EnCNC content was reached, and after that, the decrease observed was more
342 gradual as EnCNC content increased. This could confirm that the EnCNCs were embedded in
343 the WBPU matrix, and thus, the hydrophobic character of the matrix was maintained even by
344 adding hydrophilic EnCNCs. In the case of AcCNC based nanocomposites, lower water contact
345 angle values were measured, and the difference between EnCNC and AcCNC based
346 nanocomposite values was higher as AcCNC content increased. This data suggested that

12

347 AcCNCs could be more dispersed on the material surface. Therefore its hydrophilic nature was

348 held in the nanocomposite (Sun et al., 2018), agreeing with AFM results.

349   The main functional groups of the samples and the chemical interactions between both

350 nanocrystals and WBPU matrix were analyzed by FTIR. At the highest wavenumbers, between

351 3600 and 3100 cm^{-1} (**Fig. 3 a, b**), two common features of both WBPU and CNCs appeared: -

352 OH group stretching vibration related to CNCs and -NH stretching vibration associated with

353 urethane groups of WBPU. At 3340 cm^{-1}, the -NH vibration of the urethane group appeared,

354 and with the increment of CNC content, the band at 3336 cm^{-1} related to -OH groups of CNCs

355 was more pronounced (Cao, Dong, & Li, 2007; Santamaria-Echart, Ugarte, Arbelaiz, et al.,

356 2016). Comparing both nanocomposites, it could be seen that for AcCNC based

357 nanocomposites, this band appeared more discreetly. This could be caused by the lower

358 intensity of this peak in just AcCNC spectrum, where this band was reduced by the inter and

359 intramolecular changes of cellulose II and different functional groups in AcCNC, as could be

360 seen at 3486 and 3441 cm^{-1} (Han, Zhou, Wu, Liu, & Wu, 2013). Other interesting changes in

361 the nanocomposites spectra with different CNC contents were observed at the lower

362 wavenumber range. Typical cellulosic bands at 1052 and 1028 cm^{-1} related to C-O vibrations

363 were seen (Naduparambath et al., 2018), which were more pronounced as CNC content

364 increased, both for EnCNC and AcCNC based nanocomposites (**Fig. 3 a, b**). This data

365 confirmed the increment of EnCNC and AcCNC content in the WBPU nanocomposites.
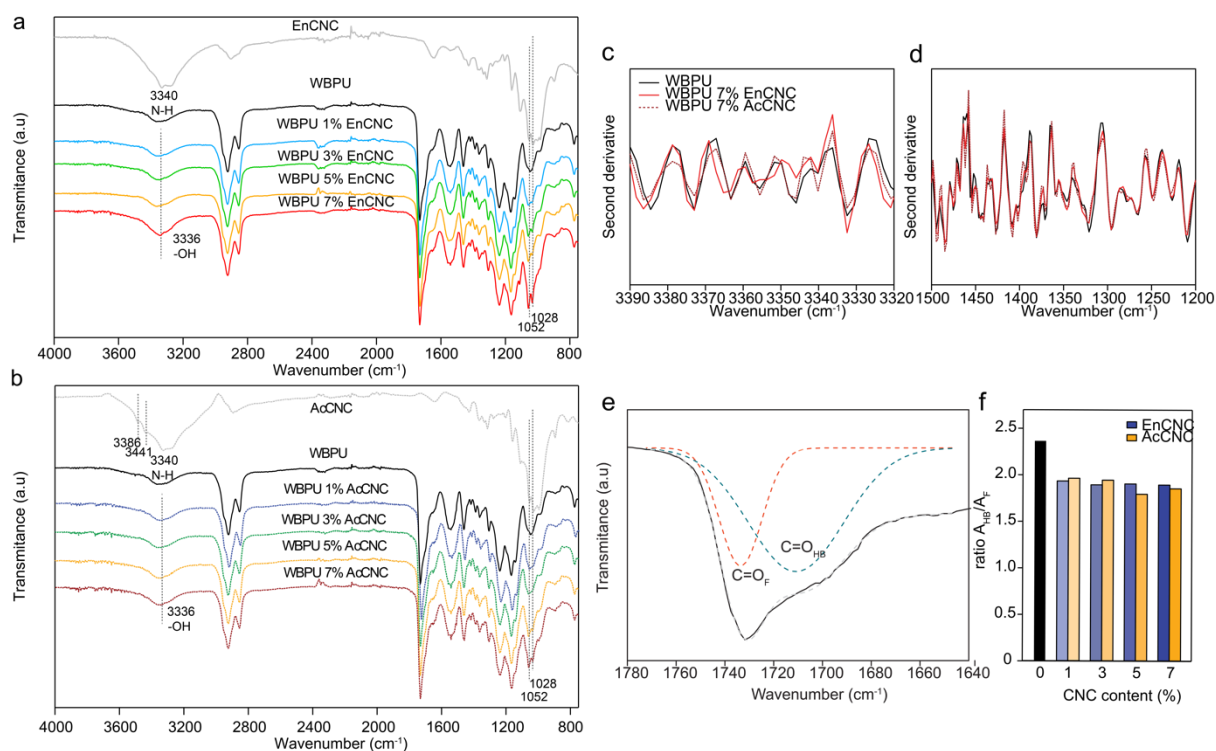
Fig. 3. FTIR analysis of WBPU/CNC nanocomposites. (a) Comparison between FTIR spectra of EnCNCs, WBPU matrix, and nanocomposites with different EnCNC contents. Spectra from 4000 to 750 cm^{-1}. (b) Comparison between FTIR spectra of AcCNCs, WBPU matrix, and nanocomposites with different AcCNC contents. Spectra from 4000 to 750 cm^{-1}. (c,d) Second derivative analysis from FTIR spectra of WBPU matrix, WBPU with 7 wt% EnCNC and AcCNC. (c) Spectra from 3390 to 3320 cm^{-1}, (d) spectra from 1500 to 1200 cm^{-1}. (e,f) Analysis of C=O groups absorption in the WBPU nanocomposites. (e) Deconvolution of C=O band of WBPU matrix as an example in two curves, one at 1730 cm^{-1} assigned to the free C=O and the second at 1705 cm^{-1} from C=O linked by hydrogen bonding. (f) The ratio between areas of hydrogen-bonded and free C=O groups (A_{HB}/A_{F}) from spectra of WBPU matrix and nanocomposites with EnCNCs and AcCNCs.

For a proper study of CNC-WBPU interactions, the second derivative spectra of the WBPU matrix and nanocomposites with 7 wt% of both CNC types were analyzed in different regions. In the 3390-3320 cm^{-1} region, the nanocomposite spectra were shifted concerning the matrix when both CNC types were present (**Fig. 3.c**), while no changes were observed in the 1500-1200 cm^{-1} region (**Fig. 3.d**). That could mean that there were new interactions between -OH groups from CNCs and -NH groups from polyurethane hard segments, by hydrogen bonding (Lei, Fang, Zhou, Li, & Pu, 2018). The differences in the displacement between nanocomposites based on different CNC types could be attributed to the different functional

14

groups presented at the EnCNC and AcCNC surfaces. The interaction between the WBPU matrix and both CNCs were also studied in the carbonyl group (C=O) region. The carbonyl band of the urethane functional group presented at 1728 cm^{-1} was deconvoluted in two Gaussian peaks, one at 1730 cm^{-1}, assigned to free C=O groups, and the other at 1710 cm^{-1} assigned to hydrogen bonded C=O. The ratio between the areas of bonded and free C=O groups curves (A_{HB}/A_F) can be used to study the evolution of hydrogen bonding in the WBPU matrix and nanocomposites (Tien & Wei, 2001). **Fig. 3.e** shows the FTIR spectrum of the WBPU matrix with the two deconvoluted curves. The A_{HB}/A_F ratio for all nanocomposites was also calculated and is represented in **Fig. 3.f.** A decrease was observed in the ratio with the addition of CNCs, in both EnCNC and AcCNC based nanocomposites. This reduction in the ratio was also found in the literature for other nanocomposites prepared with different CNC contents (Kong, Zhao, & Curtis, 2016; Pei, Malho, Ruokolainen, Zhou, & Berglund, 2011). In the matrix, WBPU particles could have a larger number of C=O groups bonded by hydrogen bonding between HSs, while in the nanocomposites, the addition of stiff and crystalline CNCs may interrupt these interactions.

Nanocomposites' thermal performance was analyzed by DSC. Thermograms from WBPU matrix, macrodiol, and nanocomposites with different EnCNC and AcCNC contents are shown in **Fig. 4 a, b**. All the thermograms measured for the WBPU matrix and nanocomposites with both CNCs were similar, however small differences that could be related to the different length and surface chemistry of EcCNC and AcCNC can be seen. In general, polyurethanes present several transitions related to the soft and hard segments. Both soft and hard segments can present ordered chains in amorphous or crystalline domains (Hu, Patil, & Hsieh, 2016). Therefore, soft segments can present a glass transition temperature far below room temperature and a melting temperature usually just around room temperature, due to its amorphous and crystalline fractions. The hard segments can present a glass transition temperature usually above room temperature and transitions related to the disruption of the hard segment assemble, which can be ordered at different scales at higher temperatures. In **Table 1S,** the thermal values for the WBPU matrix and nanocomposites with different EnCNC and AcCNC contents are shown. WBPU matrix presented a glass transition temperature at low temperatures related to the soft segment, Tg_{SS}, and a thermal relaxation at higher temperatures, between 60 to 120 °C, due to the short-range order transition of hard segments, T_{HS}. A very small peak was observed around 8-10 °C, which can be associated with the melting temperature of soft segments, Tm_{SS}, as a melting peak was also observed in the pure macrodiol thermogram.
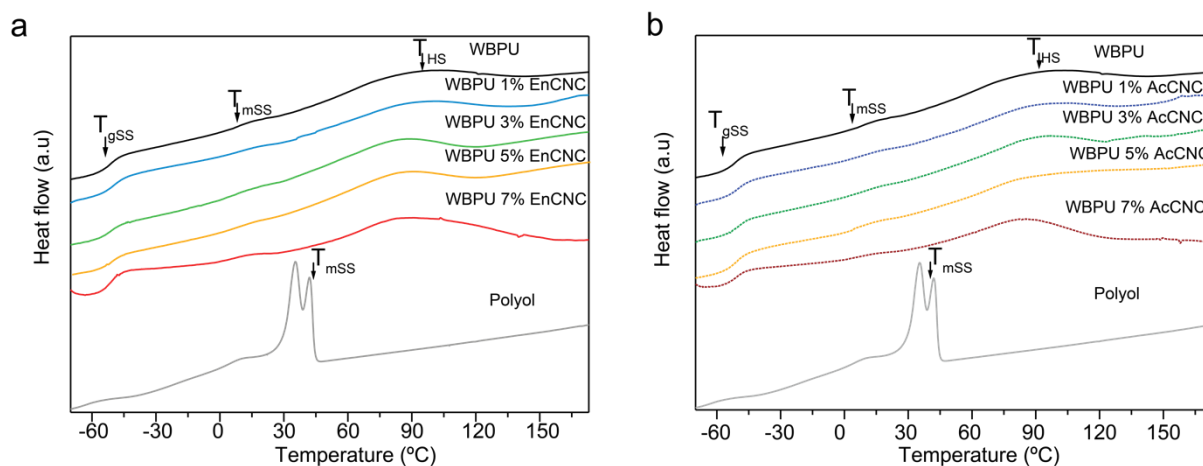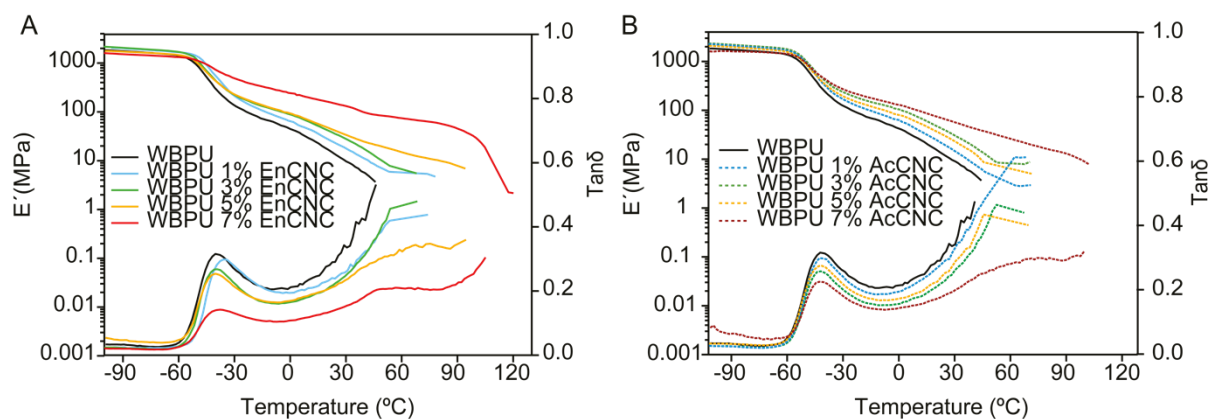
Fig. 4. DSC of WBPU/CNC nanocomposites. (a) DSC thermograms of WBPU matrix and nanocomposites with different contents of EnCNCs. (b) DSC thermograms of WBPU matrix and nanocomposites with different contents of AcCNCs.

In general, Tg_{SS} values were very similar in all the cases. The nanocomposites prepared with both types of CNCs had values around -51±2 ºC, a similar value to that found for the matrix (**Table 1S**). For the nanocomposites prepared with both types of CNCs, a reduction of T_{HS} value was observed, reaching the lowest value for the nanocomposites prepared with 7 wt% of CNCs. Similarly, a gradual loss of ΔH_{HS} value was observed for the nanocomposites. Both T_{HS} and ΔH_{HS} values reductions could mean that nanocrystals interacted with WBPU hard segments, hindering the interactions between WBPU hard segments, as also observed by FTIR. The slightly lower ΔH_{HS} values observed for the nanocomposites prepared with AcCNCs comparing with the values observed for the nanocomposites prepared with EnCNCs, at the same CNC content, could be due to the smaller size and, therefore, higher surface area that AcCNCs present, resulting in higher possible interactions among AcCNCs and HSs.

The viscoelastic behavior of the WBPU matrix and the nanocomposites prepared with different EnCNC and AcCNC contents was analyzed by DMA. The storage modulus and Tan δ curves of the WBPU matrix and nanocomposites with 1, 3, 5, and 7 wt% of EnCNC and AcCNC are given in **Fig. 5**. At low temperatures, in the glassy state, the nanocomposites showed similar E´ values compared to the WBPU matrix and did not change considerably with the addition of CNCs. A substantial decrease was observed in the E´ curves in the interval between -40 and 0 ºC that corresponds to the glassy relaxation. This drop in E´ was reflected in a maximum in the Tan δ curve, which can be associated with the Tg_{SS}. The intensity of the peak was lower for the nanocomposites when comparing with the neat WBPU. This reduction

16

443 of the intensity was more significant as CNC content increased, which can be attributed to the
444 lower content of WBPU chains available for relaxing owing to the interactions of WBPU
445 chains and CNCs in the nanocomposites (Mondragon et al., 2018). At higher temperatures, E´
446 curves showed a progressive decrease with temperature in the rubbery region due to the almost
447 irrelevant crystallinity observed for the soft segment and the lack of crystallinity in the hard
448 segment (Wu, Henriksson, Liu, & Berglund, 2007). This decrease was more pronounced for
449 the WBPU matrix, and in this way, the WBPU matrix lost its thermomechanical stability
450 earlier. Besides, all nanocomposites showed higher E´ values (**Table 2S**), enhanced with the
451 CNC content, which can be attributed to the ability of CNCs to form a stable structure through
452 hydrogen bonding interactions among nanocrystals and also with the matrix (Santamaria-
453 Echart et al., 2018; Santamaria-Echart, Ugarte, García-Astrain, et al., 2016). For the
454 nanocomposites with higher CNC contents, a considerable improvement was observed in the
455 thermomechanical stability, suggesting the formation of a percolating CNC network in which
456 stress transfer is facilitated by hydrogen-bonding between nanocrystals (Favier, Chanzy, &
457 Cavaillé, 1995). The critical CNC percolation volume fraction is calculated by 0.7/A, where A
458 is the aspect ratio of the CNCs (33 for EnCNC and 17 for AcCNC) (Favier, Dendievel, Canova,
459 Cavaille, & Gilormini, 1997). Thereby, the percolation volume fraction for EnCNC was 0.021,
460 and 0.041 for AcCNC, which corresponds to 3 and 5 wt% of EnCNC and AcCNC, respectively.
461 Note that the nanocomposites with CNC contents above the percolation threshold, WBPU 5%
462 EnCNC, WBPU 7% EnCNC and WBPU 7% AcCNC present higher thermomechanical
463 stability around the rubbery region (**Fig. 5 a, b**), thus corroborating the formation of the
464 percolating CNC network. Thermal stability was also evaluated by TGA (**Fig 4S**). As can be
465 observed, EnCNCs increase both degradations related to the hard and soft segments in the
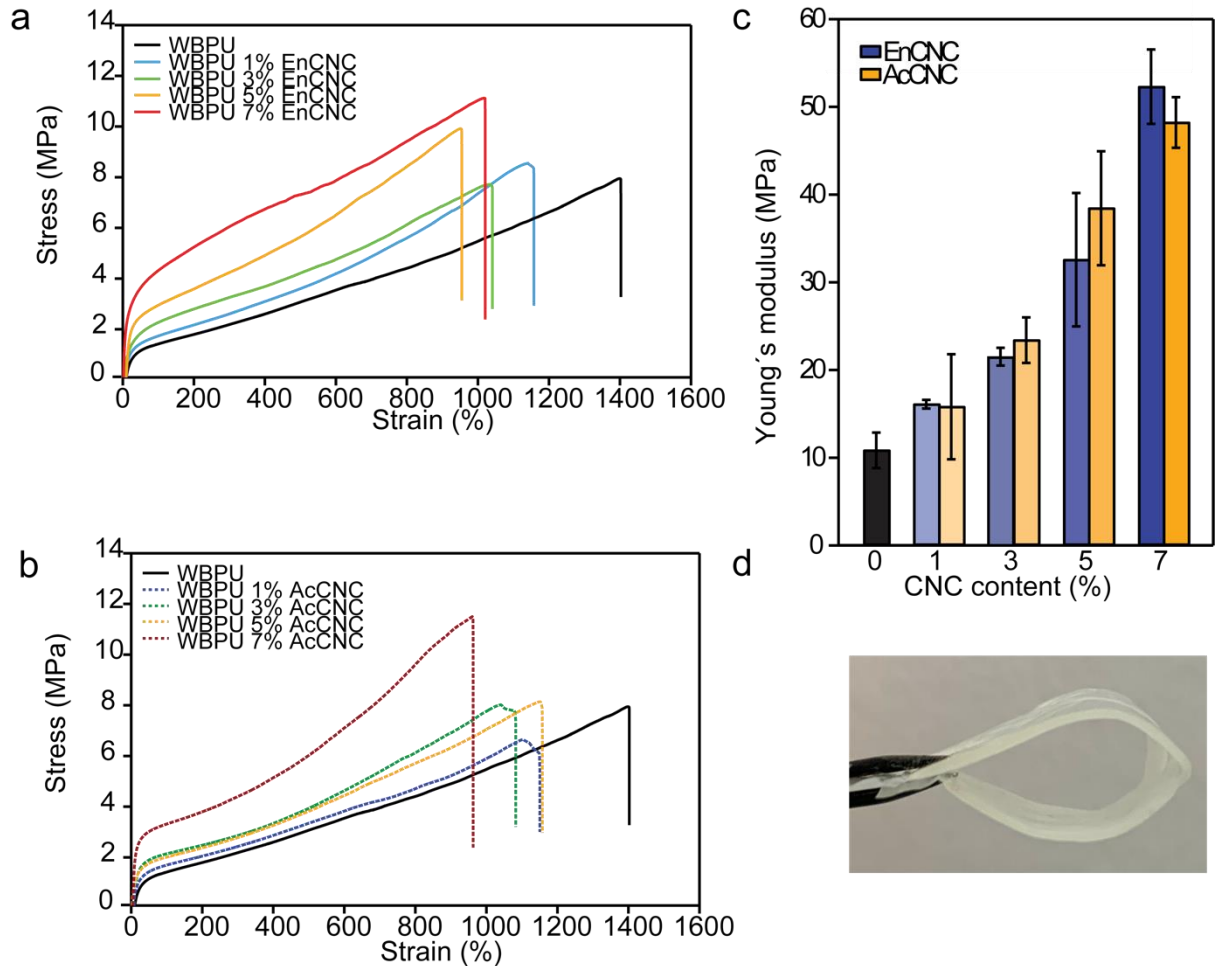466 WBPU matrix.

Fig. 5. **DMA analysis of WBPU/CNC nanocomposites**. (a) Storage modulus and Tanδ of WBPU matrix and nanocomposites with different contents of EnCNCs. (b) Storage modulus and Tanδ of WBPU matrix and nanocomposites with different contents of AcCNCs.

The mechanical properties of nanocomposites were measured by tensile tests, and the influence of both EnCNCs and AcCNCs in the WBPU matrix was analyzed. The obtained stress-strain curves are plotted in **Fig. 6 a, b,** and the Young´s modulus, yield strength, tensile strength, strain at break, and toughness values obtained from these curves are gathered in **Table 3S**. The addition of both CNC types improved the mechanical properties of the WBPU matrix. Young´s modulus and yield strength values increased with CNC content. This phenomenon was also observed in the literature, as CNC addition increased matrix stiffness (de Oliveira Patricio et al., 2013; Santamaria-Echart et al., 2018). The improvement was notable even for the nanocomposites prepared with low CNC contents, but as observed also by DMA, the addition of CNCs above the percolation threshold led to a considerable improvement in the mechanical behavior of the nanocomposites (**Fig. 6.c**), due to the formation of a percolating CNC network. It should be remarked that, although strain at break decreased with the addition of CNCs, the reduction in these values were not remarkable, suggesting good interaction between WBPU and both CNC types (Saralegi et al., 2014), and thus increasing the overall material toughness. As can be observed in **Fig. 6.d**, nanocomposites maintained good elasticity after CNCs addition. Analyzing the effect of different CNC types for nanocomposite preparation on the mechanical properties, a similar behavior was observed below the percolation threshold, and above the percolation threshold, higher Young modulus, yield strength, and tensile strength values were measured for EnCNC based nanocomposites, because the critical CNC percolation volume fraction occurs at lower values, as mentioned before. Moreover, the higher crystallinity and aspect ratio of EnCNCs compared with AcCNC also

18

influence the mechanical performance of the nanocomposites. It was seen in the literature that the source and physicochemical properties of nanocelluloses affected the final properties of the materials (Siqueira, Bras, & Dufresne, 2008).


Fig. 6. Mechanical analysis of WBPU/CNC nanocomposites. (a,b) Stress-strain curves of WBPU matrix and nanocomposites with different contents of EnCNCs and AcCNCs. (c) Young´s modulus of WBPU matrix and nanocomposites with different contents of EnCNCs and AcCNCs. The average values and standard deviations were calculated from five independent experiments. d) Photograph of a folded strip of the nanocomposite with 7 wt% of EnCNCs.

3.3. WBPU/CNC as paper coating

The role of WBPU/EnCNC mixtures as coating material was analyzed during this work after proving that EnCNCs improve WBPU properties. The satin paper was coated with 1, 2, and 3 layers of the same formulation using the nanocomposites prepared with the same AcCNC and

506   EnCNC content (1, 3, 5, and 7 wt%). Coatings were applied by hand with the K-bars producing

507   a transparent layer of around 5 µm of thickness, reaching a thickness of 15 µm for the final

508   samples coated with 3 layers. The addition of both types of CNCs did not affect the coating's

509   transparency, as also observed previously in the films prepared with those nanocomposites.

510   The adhesion of the coatings over the films was measured by adhesion tests, cutting the samples

511   by the edge cutting tool to produce 100 small squares over the films (**Fig. 7.a**). According to

512   the standard test method ASTM D3359, WBPU based coating presented high adhesion with 1,

513   2 and 3 layers, with few small detached zones in some squares, reaching a 4B grade. Coatings

514   prepared with both AcCNC and EnCNC based nanocomposites also showed good adhesion

515   performance, maintaining in all the samples the 4B value, as the control sample. This result

516   indicated that EnCNC/WBPU nanocomposites could be used as strong adhesives (Heinrich,

517   2019).
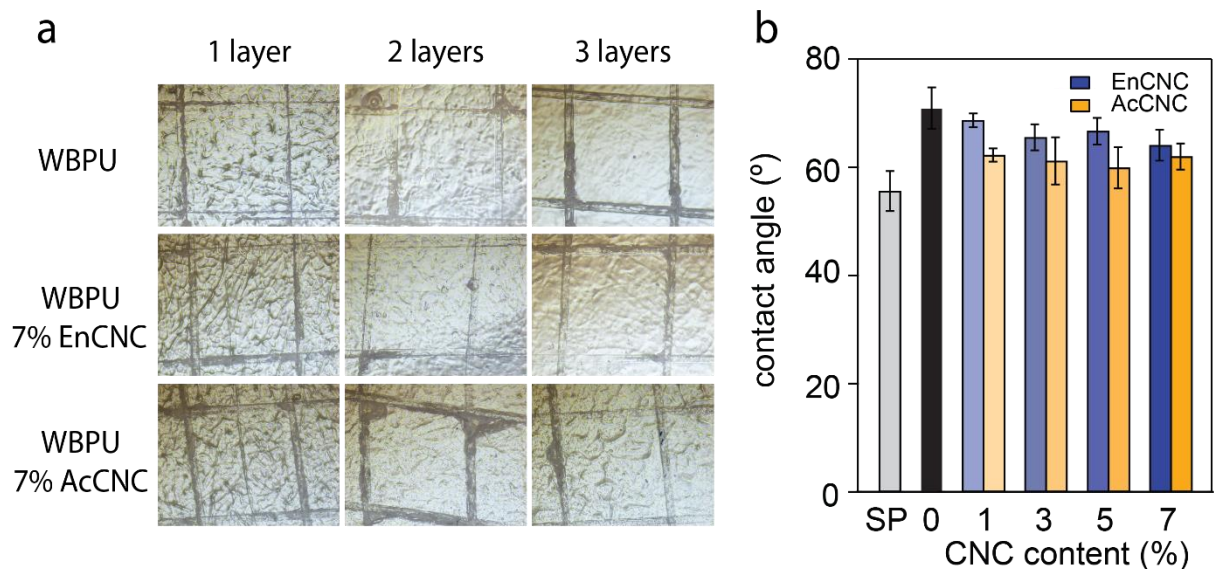
518

519   **Fig. 7. Adhesion tests and WCA angle values of WBPU/CNC based coatings.** (a)

520   Microscopy images of adhesion tests performed to WBPU, WBPU 7% EnCNC, and WBPU

521   7% AcCNC coatings over the satin paper with thicknesses consisting of 1, 2, and 3 layers. (b)

522   WCA values of coatings prepared with 3 layers of WBPU, WBPU + EnCNC, and WBPU +

523   AcCNC over the satin paper (SP). The average contact angle values and standard deviations

524   were calculated from ten independent experiments.

525   The water contact angle was also measured over the coatings to evaluate their

526   hydrophobicity. WBPU based coating increased the hydrophobicity of the satin paper, and

527   there were no significant differences between layers (**Fig. 5S**). Regarding coatings prepared

528   with nanocomposites based on both types of CNCs, a decrease was observed in the surface

529   hydrophobicity. Still, in all cases, it was higher than the behavior observed in the satin paper

530   itself. Furthermore, the coatings prepared with 3 layers showed the sharpest drop (**Fig. 7.b**).

531   Coatings prepared with AcCNC based nanocomposites presented the higher hydrophilicity due

532   to the hydrophilic behavior of sulfate groups. In contrast, coatings prepared with EnCNC based

533   nanocomposites showed similar values to WBPU control. These results are consistent with

534   those concluded from the films prepared with WBPU/AcCNC and WBPU/EnCNC

535   nanocomposites.

536   The abrasion resistance of the coatings was also evaluated using a Taber abrader (**Fig. 8.a**).

537   All the formulations were tested, and **Fig. 8.b** shows the ones with higher abrasion resistance.

538   The abrasion resistance improved with the number of layers as well as the addition of both

539   CNCs. 5 wt% EnCNC addition was enough to improve the abrasion resistance of the WBPU

540   matrix, while in the case of AcCNCs, an addition of 7 wt% was needed to obtain similar results.

541   The bigger size of EnCNCs, and the good interactions observed between EnCNCs and WBPU

542   chains in the nanocomposite films, as well as the higher thermomechanical stability, could

543   explain these results. SEM images of the abraded coating surface after abrasion test (**Fig. 8.c**)

544   showed that more significant breaks were produced for the coatings prepared with the WBPU

545   matrix. WBPU/EnCNC based coatings presented the smaller fractured areas, and the satin

546   paper was not damaged by the abrasion wheels, reaching the higher reinforcement with three

547   layers of WBPU/EnCNC based coating.
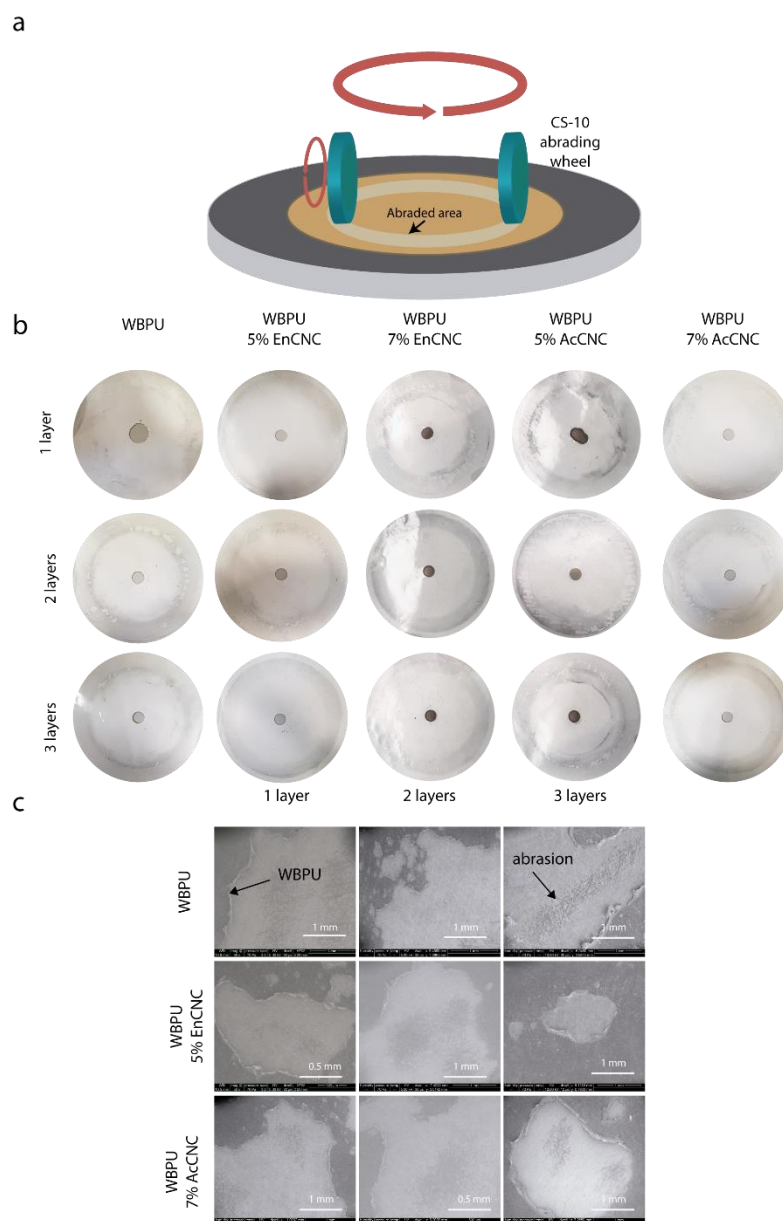
Fig. 8. Abrasion tests on WBPU and WBPU/CNC based coatings. (a) Scheme of mechanical abrasion of the coatings using Taber abrader with CS-10 wheels. (b) WBPU, WBPU 5 and 7 % EnCNC and AcCNC coatings with thicknesses consisting of 1, 2, and 3 layers after 50 cycles of abrasion test. (c) SEM images of the coatings after the abrasion test.

3.4. WBPU/CNC as electrospun nanocomposite mats

WBPU/CNC formulations were also evaluated for a second application as electrospun nanocomposite mats. In these experiments, POE assisted WBPU and WBPU/CNC based microfibers were electrospun, removing after that POE by water washing. WBPU/POE and WBPU/CNC/POE (with both CNC types) based formulations were loaded into the syringe to

fabricate electrospun mats as shown in the scheme (**Fig. 9.a**). The morphology of the mats was analyzed by SEM after and before POE removal (**Fig. 9.b**). Before the washing treatment, a very homogeneous dispersion of fibers was produced in all cases, remarking the good spinnability of POE assisted WBPU and WBPU/CNC formulations. No fiber agglomerations were visible in the images, neither in the electrospun WBPU mats nor in the electrospun nanocomposite mats, remarking the good integration of both types of CNCs. All fibers showed similar diameters and in the nanoscale. The WBPU based mats measured 829.5±112.8 nm, WBPU/EnCNC based mats 715.1±160.3 nm, and WBPU/AcCNC based ones 761.6±97.2 nm. When POE was removed, fibers showed higher diameter values, which can be due to the swelling with water molecules during POE removal and to the drying process itself, which occurs horizontally. For the WBPU sample, the diameter increased to 1264.5±168.3 nm. However, the fibers hold their shape better for the mats based on WBPU/EnCNC and WBPU/AcCNC. WBPU/EnCNC based mats presented the thinner fibers, 890.8±150.1 nm, in comparison with 1097±214 nm for WBPU/AcCNC based mats. The good interaction between WBPU and CNCs already observed for the nanocomposite films helped maintain the fibers' shape. Although sulfate groups on the AcCNC surface help spinnability as they could act as polyelectrolytes (Bellani et al., 2016; Santamaria-Echart et al., 2017), they also increase the hydrophilicity of the fibers and their affinity to water, being more removable during the washing process. Therefore, the lower dispersibility of EnCNCs in water, as shown in Figure S1, and the higher interactions with WBPU matrix could better hold the shape of the fibers.
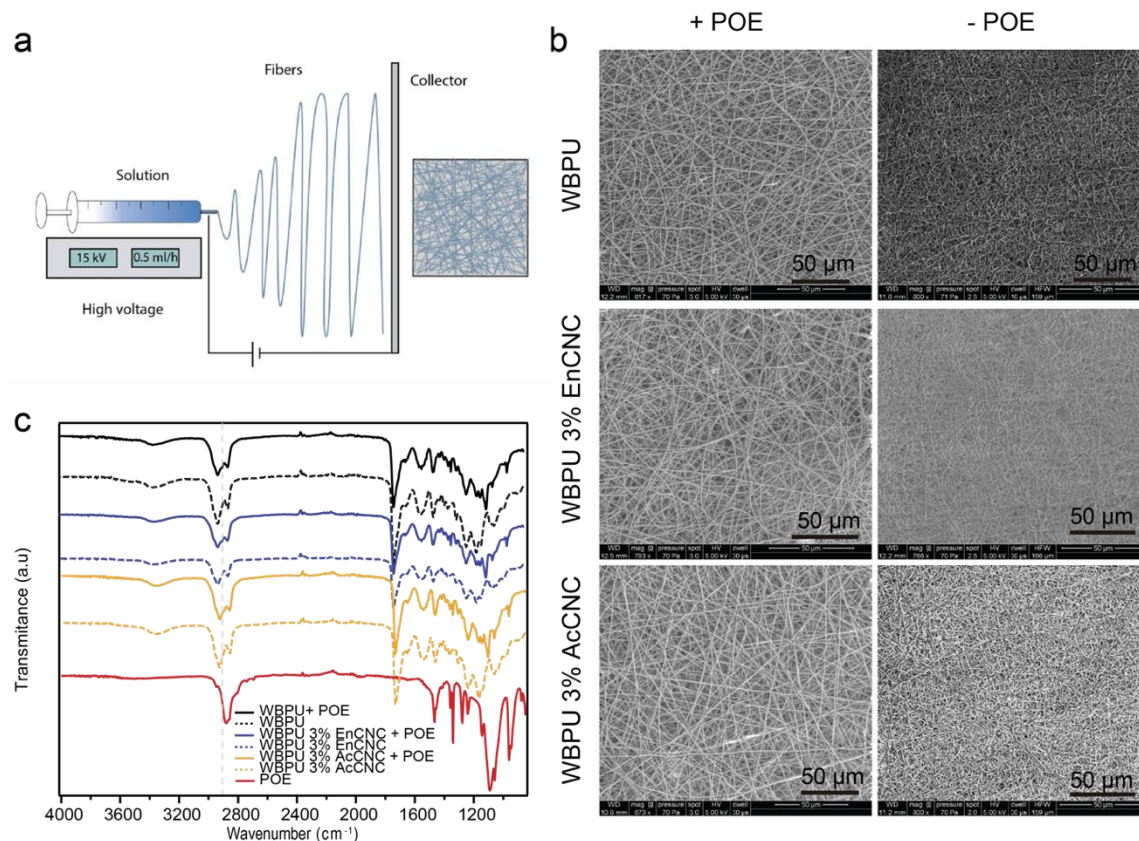
Fig. 9. WBPU/CNC electrospinning. (a) Scheme of electrospinning method. The collector was placed at 20 cm from the syringe needle, (b) SEM images of WBPU, WBPU 3% EnCNC and WBPU 3% AcCNC before and after POE removal. (c) FTIR analysis of POE, WBPU, WBPU 3% EnCNC, and WBPU 3% AcCNC mats before and after POE removal. Spectra from 4000 to 850 cm^{-1}.

FTIR spectroscopy was used to ensure POE removal with the washing process. Before and after the washing process, WBPU based mats presented different bands (**Fig. 9.c**). Observing the spectra of washed samples, after the washing process, some bands are not presented, specifically, the ones associated with POE at 1340, 1280, 1006, and 960 cm^{-1} (**Fig. 6S**) (Wang, Chang, Ahmad, & Li, 2016). This analysis and the morphological change of the mats show the successful removal of POE and maintaining CNCs in the mats as observed in FTIR spectra where bands related to CNC at 1052 and 1028 cm^{-1} can be appreciated (**Fig. 7S**). The hydrophobicity of the mats was analyzed by WCA measurements. Before the washing process, the mats could not be assayed due to the high hydrophilicity of POE. Nevertheless, after the washing process, the hydrophobicity increased for all the mats, and is possible to measure their WCA. WBPU based mats presented contact angle values around 80° (**Fig. 8S**). This value was higher in comparison with the values obtained for WBPU and WBPU nanocomposites films

24

and coatings due to the rough surface formed by random fiber deposition that leads to higher hydrophobicity. When EnCNCs were present in the mats, the contact angle values slightly decrease. This decrease was more pronounced when AcCNCs were present, showing the tendency also observed for films and coatings.

4. Conclusion

WBPU nanocomposites with different EnCNC and commercial AcCNC contents were fabricated. The results showed that small CNC addition to the WBPU matrix had a remarkable impact on the material's mechanical and thermal properties. EnCNCs improvement was the same or even better in some properties than AcCNC. The differences observed between the nanocomposites, concerning both CNC type and content, were explained by the different physicochemical properties that each CNC present. The results of this work proved the importance of CNC isolation method in the final application performance. Moreover, it should be highlighted that by using EnCNCs as reinforcement for the preparation of nanocomposites based on WBPU, a greener material would be produced than in the case of using AcCNCs. These WBPU/EnCNC mixtures' versatility was tested as coatings for a paper substrate and electrospun mats. WBPU/EnCNC based coatings showed higher resistance to mechanical abrasion than those based on WBPU/AcCNC. Besides, the electrospun mats obtained using WBPU/EnCNC formulations presented fibers that hold better their structure after the washing process in comparison with WBPU/AcCNC based fibers.

Competing financial interests

The authors declare no competing interests.

Author Contributions

Borja Alonso-Lerma: Methodology, Investigation, Writing, Visualization, Formal analysis**.** **Izaskun Larraza:** Methodology, Investigation. **Leire Barandiaran:** Methodology, Investigation. **Lorena Ugarte:** Methodology, Investigation. **Ainara Saralegi***:* Methodology, Investigation. **Maria Angeles Corcuera:** Methodology, Investigation. **Raul Perez-Jimenez:** Conceptualization, Methodology, Supervision, Writing, Visualization, Formal analysis. Funding acquisition. **Arantxa Eceiza:** Conceptualization, Methodology, Supervision, Writing, Visualization, Formal analysis. Funding acquisition.

References:

Alonso-Lerma, B., Barandiaran, L., Ugarte, L., Larraza, I., A, R., Olmos-Juste, R., . . . Perez-Jimenez, R. (2020). High performance crystalline nanocellulose using an ancestral endoglucanase. *Communications Materials*.

Alonso-Lerma, B., Barandiaran, L., Ugarte, L., Larraza, I., Reifs, A., Olmos-Juste, R., . . . Eceiza, A. (2020). High performance crystalline nanocellulose using an ancestral endoglucanase. *Communications Materials,* 1(1), 1-10.

Amin, K., Annamalai, P., Morrow, I., & Martin, D. (2015). Production of cellulose nanocrystals via a scalable mechanical method. RSC Adv 5: 57133–57140.

Bellani, C. F., Pollet, E., Hebraud, A., Pereira, F. V., Schlatter, G., Avérous, L., . . . Branciforti, M. C. (2016). Morphological, thermal, and mechanical properties of poly (ε-caprolactone)/poly (ε-caprolactone)-grafted-cellulose nanocrystals mats produced by electrospinning. *J. Appl. Polym. Sci.,* 133(21).

Cao, X., Dong, H., & Li, C. M. (2007). New nanocomposite materials reinforced with flax cellulose nanocrystals in waterborne polyurethane. *Biomacromolecules,* 8(3), 899-904.

Chowdhury, R. A., Clarkson, C. M., Shrestha, S., El Awad Azrak, S. M., Mavlan, M., & Youngblood, J. P. (2019). High-Performance Waterborne Polyurethane Coating Based on a Blocked Isocyanate with Cellulose Nanocrystals (CNC) as the Polyol. *ACS Applied Polymer Materials,* 2(2), 385-393.

de Oliveira Patricio, P. S., Pereira, I. M., da Silva, N. C. F., Ayres, E., Pereira, F. V., & Oréfice, R. L. (2013). Tailoring the morphology and properties of waterborne polyurethanes by the procedure of cellulose nanocrystal incorporation. *Eur. Polym. J.,* 49(12), 3761-3769.

Dufresne, A. (2013). Nanocellulose: a new ageless bionanomaterial. *Materials today,* 16(6), 220-227.

Favier, V., Chanzy, H., & Cavaillé, J. (1995). Polymer nanocomposites reinforced by cellulose whiskers. *Macromolecules,* 28(18), 6365-6367.

Favier, V., Dendievel, R., Canova, G., Cavaille, J., & Gilormini, P. (1997). Simulation and modeling of three-dimensional percolating structures: case of a latex matrix reinforced by a network of cellulose fibers. *Acta Materialia,* 45(4), 1557-1565.

Filson, P. B., Dawson-Andoh, B. E., & Schwegler-Berry, D. (2009). Enzymatic-mediated production of cellulose nanocrystals from recycled pulp. *Green Chemistry,* 11(11), 1808-1814.

Fortunati, E., Peltzer, M., Armentano, I., Torre, L., Jiménez, A., & Kenny, J. (2012). Effects of modified cellulose nanocrystals on the barrier and migration properties of PLA nano-biocomposites. *Carbohydr. Polym.,* 90(2), 948-956.

Gao, Z., Peng, J., Zhong, T., Sun, J., Wang, X., & Yue, C. (2012). Biocompatible elastomer of waterborne polyurethane based on castor oil and polyethylene glycol with cellulose nanocrystals. *Carbohydr. Polym.,* 87(3), 2068-2075.

Habibi, Y., Lucia, L. A., & Rojas, O. J. (2010). Cellulose nanocrystals: chemistry, self-assembly, and applications. *Chemical reviews,* 110(6), 3479-3500.

Han, J., Zhou, C., Wu, Y., Liu, F., & Wu, Q. (2013). Self-assembling behavior of cellulose nanoparticles during freeze-drying: effect of suspension concentration, particle size, crystal structure, and surface charge. *Biomacromolecules,* 14(5), 1529-1540.

Heinrich, L. A. (2019). Future opportunities for bio-based adhesives–advantages beyond renewability. *Green chemistry,* 21(8), 1866-1888.

Henriksson, M., Henriksson, G., Berglund, L., & Lindström, T. (2007). An environmentally friendly method for enzyme-assisted preparation of microfibrillated cellulose (MFC) nanofibers. *Eur. Polym. J.,* 43(8), 3434-3441.

Hormaiztegui, M. E. V., Daga, B., Aranguren, M. I., & Mucci, V. (2020). Bio-based waterborne polyurethanes reinforced with cellulose nanocrystals as coating films. *Progress in Organic Coatings,* 144, 105649.

Hormaiztegui, M. V., Mucci, V. L., & Aranguren, M. I. (2019). Composite films obtained from a waterborne biopolyurethane. Incorporation of tartaric acid and nanocellulose. *Industrial Crops and Products,* 142, 111879.

Hu, W., Patil, N. V., & Hsieh, A. J. (2016). Glass transition of soft segments in phase-mixed poly (urethane urea) elastomers by time-domain 1H and 13C solid-state NMR. *Polymer,* 100, 149-157.

Hung, K.-C., Tseng, C.-S., Dai, L.-G., & Hsu, S.-h. (2016). Water-based polyurethane 3D printed scaffolds with controlled release function for customized cartilage tissue engineering. *Biomaterials,* 83, 156-168.

Jardin, J. M., Zhang, Z., Hu, G., Tam, K. C., & Mekonnen, T. H. (2020). Reinforcement of rubber nanocomposite thin sheets by percolation of pristine cellulose nanocrystals. *International Journal of Biological Macromolecules*.

Jaudouin, O., Robin, J. J., Lopez-Cuesta, J. M., Perrin, D., & Imbert, C. (2012). Ionomer-based polyurethanes: a comparative study of properties and applications. *Polym. Int.,* 61(4), 495-510.

Kallel, F., Bettaieb, F., Khiari, R., García, A., Bras, J., & Chaabouni, S. E. (2016). Isolation and structural characterization of cellulose nanocrystals extracted from garlic straw residues. *Industrial Crops and Products,* 87, 287-296.

Kong, X., Zhao, L., & Curtis, J. M. (2016). Polyurethane nanocomposites incorporating biobased polyols and reinforced with a low fraction of cellulose nanocrystals. *Carbohydr. Polym.,* 152, 487-495.

Lei, W., Fang, C., Zhou, X., Li, Y., & Pu, M. (2018). Polyurethane elastomer composites reinforced with waste natural cellulosic fibers from office paper in thermal properties. *Carbohydr. Polym.*

Lei, W., Zhou, X., Fang, C., Song, Y., & Li, Y. (2019). Eco-friendly waterborne polyurethane reinforced with cellulose nanocrystal from office waste paper by two different methods. *Carbohydrate polymers,* 209, 299-309.

Lin, N., & Dufresne, A. (2014). Surface chemistry, morphological analysis and properties of cellulose nanocrystals with gradiented sulfation degrees. *Nanoscale,* 6(10), 5384-5393.

Liu, H., Liu, D., Yao, F., & Wu, Q. (2010). Fabrication and properties of transparent polymethylmethacrylate/cellulose nanocrystals composites. *Bioresource Technology,* 101(14), 5685-5692.

Lu, Y., & Larock, R. C. (2008). Soybean-oil-based waterborne polyurethane dispersions: effects of polyol functionality and hard segment content on properties. *Biomacromolecules,* 9(11), 3332-3340.

Madbouly, S. A., Xia, Y., & Kessler, M. R. (2013). Rheological behavior of environmentally friendly castor oil-based waterborne polyurethane dispersions. *Macromolecules,* 46(11), 4606-4616.

Mondragon, G., Santamaria-Echart, A., Hormaiztegui, M., Arbelaiz, A., Peña-Rodriguez, C., Mucci, V., . . . Eceiza, A. (2018). Nanocomposites of waterborne polyurethane reinforced with cellulose nanocrystals from sisal fibres. *J. Polym. Environ.,* 26(5), 1869-1880.

Moon, R. J., Martini, A., Nairn, J., Simonsen, J., & Youngblood, J. (2011). Cellulose nanomaterials review: structure, properties and nanocomposites. *Chem. Soc. Rev.,* 40(7), 3941-3994.

Naduparambath, S., Jinitha, T., Shaniba, V., Sreejith, M., Balan, A. K., & Purushothaman, E. (2018). Isolation and characterisation of cellulose nanocrystals from sago seed shells. *Carbohydr. Polym.,* 180, 13-20.

Nelson, A. M., & Long, T. E. (2014). Synthesis, Properties, and Applications of Ion-Containing Polyurethane Segmented Copolymers. *Macromol. Chem. Phys.,* 215(22), 2161-2174.

Park, S.-A., Eom, Y., Jeon, H., Koo, J. M., Lee, E. S., Jegal, J., . . . Park, J. (2019). Preparation of synergistically reinforced transparent bio-polycarbonate nanocomposites with highly dispersed cellulose nanocrystals. *Green chemistry,* 21(19), 5212-5221.

Pei, A., Malho, J.-M., Ruokolainen, J., Zhou, Q., & Berglund, L. A. (2011). Strong nanocomposite reinforcement effects in polyurethane elastomer with low volume fraction of cellulose nanocrystals. *Macromolecules,* 44(11), 4422-4427.

Perez-Liminana, M. A., Aran-Ais, F., Torró-Palau, A. M., Orgilés-Barceló, A. C., & Martín-Martínez, J. M. (2005). Characterization of waterborne polyurethane adhesives containing different amounts of ionic groups. *Int. J. Adhes. Adhes.,* 25(6), 507-517.

Rahman, M. M., Suleiman, R., & Do Kim, H. (2017). Effect of functionalized multiwalled carbon nanotubes on weather degradation and corrosion of waterborne polyurethane coatings. *Korean Journal of Chemical Engineering,* 34(9), 2480-2487.

Rahman, M. M., Zahir, M., Haq, M., Shehri, D. A. A., & Kumar, A. M. (2018). Corrosion Inhibition Properties of Waterborne Polyurethane/Cerium Nitrate Coatings on Mild Steel. *Coatings,* 8(1), 34.

Remya, V., Patil, D., Abitha, V., Rane, A. V., & Mishra, R. K. (2016). Biobased materials for polyurethane dispersions. *Chem. Int.,* 2(3), 158-167.

Santamaria-Echart, A., Fernandes, I., Ugarte, L., Barreiro, F., Arbelaiz, A., Corcuera, M. A., & Eceiza, A. (2018). Waterborne polyurethane-urea dispersion with chain extension step in homogeneous medium reinforced with cellulose nanocrystals. *Compos. B. Eng.,* 137, 31-38.

Santamaria-Echart, A., Ugarte, L., Arbelaiz, A., Gabilondo, N., Corcuera, M. A., & Eceiza, A. (2016). Two different incorporation routes of cellulose nanocrystals in waterborne polyurethane nanocomposites. *Eur. Polym. J.,* 76, 99-109.

Santamaria-Echart, A., Ugarte, L., García-Astrain, C., Arbelaiz, A., Corcuera, M. A., & Eceiza, A. (2016). Cellulose nanocrystals reinforced environmentally-friendly waterborne polyurethane nanocomposites. *Carbohydr. Polym.,* 151, 1203-1209.

Santamaria-Echart, A., Ugarte, L., Gonzalez, K., Martin, L., Irusta, L., Gonzalez, A., . . . Eceiza, A. (2017). The role of cellulose nanocrystals incorporation route in waterborne polyurethane for preparation of electrospun nanocomposites mats. *Carbohydr. Polym.,* 166, 146-155.

Saralegi, A., Gonzalez, M. L., Valea, A., Eceiza, A., & Corcuera, M. A. (2014). The role of cellulose nanocrystals in the improvement of the shape-memory properties of castor oil-based segmented thermoplastic polyurethanes. *Compos. Sci. Techol.,* 92, 27-33.

740 Saralegi, A., Rueda, L., Fernández-d'Arlas, B., Mondragon, I., Eceiza, A., & Corcuera, M. A. (2013). Thermoplastic
741   polyurethanes from renewable resources: effect of soft segment chemical structure and molecular weight on
742   morphology and final properties. *Polymer international, 62*(1), 106-115.
743 Siqueira, G., Bras, J., & Dufresne, A. (2008). Cellulose whiskers versus microfibrils: influence of the nature of the nanoparticle
744   and its surface functionalization on the thermal and mechanical properties of nanocomposites.
745   *Biomacromolecules, 10*(2), 425-432.
746 Standard, A. (2010). D4060,''Standard Test Method for Abrasion Resistance of Organic Coatings by the Taber Abraser''. *West*
747   *Conshohocken (PA): ASTM International*.
748 Sun, X., Mei, C., French, A. D., Lee, S., Wang, Y., & Wu, Q. (2018). Surface wetting behavior of nanocellulose-based composite
749   films. *Cellulose, 25*(9), 5071-5087.
750 Tien, Y., & Wei, K. (2001). High-tensile-property layered silicates/polyurethane nanocomposites by using reactive silicates as
751   pseudo chain extenders. *Macromolecules, 34*(26), 9045-9052.
752 Trache, D., Hussin, M. H., Haafiz, M. M., & Thakur, V. K. (2017). Recent progress in cellulose nanocrystals: sources and
753   production. *Nanoscale, 9*(5), 1763-1786.
754 Urbina, L., Alonso-Varona, A., Saralegi, A., Palomares, T., Eceiza, A., Corcuera, M. Á., & Retegi, A. (2019). Hybrid and
755   biocompatible cellulose/polyurethane nanocomposites with water-activated shape memory properties.
756   *Carbohydrate polymers, 216*, 86-96.
757 Voronova, M. I., Surov, O. V., Guseinov, S. S., Barannikov, V. P., & Zakharov, A. G. (2015). Thermal stability of polyvinyl
758   alcohol/nanocrystalline cellulose composites. *Carbohydrate polymers, 130*, 440-447.
759 Wang, J.-C., Chang, M.-W., Ahmad, Z., & Li, J.-S. (2016). Fabrication of patterned polymer-antibiotic composite fibers via
760   electrohydrodynamic (EHD) printing. *J. Drug Deliv. Sci. Technol., 35*, 114-123.
761 Wu, Q., Henriksson, M., Liu, X., & Berglund, L. A. (2007). A high strength nanocomposite based on microcrystalline cellulose
762   and polyurethane. *Biomacromolecules, 8*(12), 3687-3692.
763 Yang, Z., & Wu, G. (2020). Effects of soft segment characteristics on the properties of biodegradable amphiphilic waterborne
764   polyurethane prepared by a green process. *Journal of Materials Science, 55*(7), 3139-3156.
765 Yarbrough, J. M., Zhang, R., Mittal, A., Vander Wall, T., Bomble, Y. J., Decker, S. R., . . . Ciesielski, P. N. (2017). Multifunctional
766   cellulolytic enzymes outperform processive fungal cellulases for coproduction of nanocellulose and biofuels. *Acs*
767   *Nano, 11*(3), 3101-3109.
768 Yoo, H. J., & Kim, H. D. (2008). Characteristics of waterborne polyurethane/poly (N-vinylpyrrolidone) composite films for
769   wound-healing dressings. *J. Appl. Polym. Sci., 107*(1), 331-338.
770 Zheng, H., Pan, M., Wen, J., Yuan, J., Zhu, L., & Yu, H. (2019). Robust, Transparent and Superhydrophobic Coating Fabricated
771   with Waterborne Polyurethane and Inorganic Nanoparticle Composites. *Ind. Eng. Chem. Res.*

772

773